Distance, Energy, and Variability of Quasar Outflows: Two *HST*/COS Epochs of LBQS 1206+1052[*]

Timothy R. Miller[1] , Nahum Arav[1], Xinfeng Xu[1] , Gerard A. Kriss[2] , Rachel J. Plesha[2], Chris Benn[3], and Guilin Liu[4,5]

[1] Department of Physics, Virginia Polytechnic Institute and State University, Blacksburg, VA 24061, USA
[2] Space Telescope Science Institute, 3700 San Martin Drive, Baltimore, MD 21218, USA
[3] Isaac Newton Group, Apartado 321, E-38700 Santa Cruz del La Palma, Spain
[4] CAS Key Laboratory for Research in Galaxies and Cosmology, Department of Astronomy, University of Science and Technology of China, Hefei 230026, People's Republic of China
[5] School of Astronomy and Space Sciences, University of Science and Technology of China, Hefei 230026, People's Republic of China
Received 2018 June 28; revised 2018 July 29; accepted 2018 August 3; published 2018 September 25

Abstract

We analyze new *HST*/COS spectra for two quasar absorption outflows seen in the quasi-stellar object LBQS 1206 +1052. These data cover, for the first time, absorption troughs from S IV, Si II, and P V. From the ratio of the S IV* to S IV column densities, we measure the electron number density of the higher-velocity ($-1400\,\mathrm{km\,s^{-1}}$, v1400) outflow to be $\log(n_e) = 4.23^{+0.09}_{-0.09}\,\mathrm{cm^{-3}}$ and constrain the lower-velocity ($-730\,\mathrm{km\,s^{-1}}$, v700) outflow to $\log(n_e) > 5.3\,\mathrm{cm^{-3}}$. The n_e associated with the higher-velocity outflow is an order of magnitude larger than reported in prior work. We find that the previous measurement was unreliable since it was based on density-sensitive absorption troughs that were likely saturated. Using photoionization models, we determine the best χ^2-minimization fit for the ionization parameter and hydrogen column density of the higher-velocity outflow: $\log(U_{\mathrm{H}}) = -1.73^{+0.21}_{-0.12}$ and $\log(N_{\mathrm{H}}) = 21.03^{+0.25}_{-0.15}\,\mathrm{cm^{-2}}$, respectively. We calculate from U_{H} and n_e a distance of 500^{+100}_{-110} pc from the central source to the outflow. Using an SED attenuated by the v700 outflow yields a two-phase photoionization solution for the v1400 outflow, separated by a $\Delta U \approx 0.7$. Otherwise, the resultant distance, mass flux, and kinetic luminosity are similar to the unattenuated case. However, the attenuated analysis has significant uncertainties due to a lack of constraints on the v700 outflow in 2017.

Key words: galaxies: active – galaxies: kinematics and dynamics – ISM: jets and outflows – quasars: absorption lines – quasars: general – quasars: individual (LBQS 1206+1052)

1. Introduction

A large fraction (∼20%–40% of all quasars; Hewett & Foltz 2003; Dai et al. 2008; Knigge et al. 2008) of quasar spectra have blueshifted absorption troughs with respect to the rest frame of the quasar, indicative of outflowing material. These outflows are typically classified according to the widths of their absorption troughs. Widths greater than $2000\,\mathrm{km\,s^{-1}}$, between 500 and $2000\,\mathrm{km\,s^{-1}}$, and less than $500\,\mathrm{km\,s^{-1}}$ are labeled broad absorption lines (BALs), mini-broad absorption lines (mini-BALs), and narrow absorption lines (NALs), respectively (e.g., Weymann et al. 1991; Aldcroft et al. 1994; Reichard et al. 2003; Vestergaard 2003; Hamann & Sabra 2004; Trump et al. 2006). These intrinsic outflows are prime candidates for producing active galactic nucleus (AGN) feedback processes: curtailing the growth of the host galaxy (e.g., Ciotti et al. 2009; Hopkins et al. 2009; Schaye et al. 2015; Choi et al. 2017; Peirani et al. 2017), explaining the relationship between the masses of the central black hole and the host galaxy (e.g., Silk & Rees 1998; Blandford & Begelman 2004; Booth & Schaye 2009; Hopkins et al. 2009; Dubois et al. 2014; Rosas-Guevara et al. 2015; Volonteri et al. 2016; Anglés-Alcázar et al. 2017), and chemical enrichment of the intergalactic and intracluster medium (e.g., Scannapieco & Oh 2004; Khalatyan et al. 2008; Tornatore et al. 2010; Barai et al. 2011; Taylor & Kobayashi 2015).

A crucial parameter needed to determine the impact of these outflows is their distance from the central source (R). These distances can be inferred from simultaneously determining the hydrogen number density (n_{H}) and ionization parameter (U_{H}) of the outflow. To date, ∼20 distances for quasar outflows have been determined using this method by our group (e.g., de Kool et al. 2001, 2002; Korista et al. 2008; Moe et al. 2009; Bautista et al. 2010; Dunn et al. 2010; Aoki et al. 2011; Edmonds et al. 2011; Arav et al. 2012, 2013, 2015; Borguet et al. 2012b, 2013; Chamberlain et al. 2015; Chamberlain & Arav 2015; Xu et al. 2018) and others (e.g., Hamann et al. 2001; Gabel et al. 2005; Finn et al. 2014; Lucy et al. 2014). These distances are in the range of parsecs to tens of kiloparsecs, many orders of magnitude more distant than accretion disk wind models predict (e.g., Murray et al. 1995; Proga et al. 2000; Proga & Kallman 2004).

AGN outflows also show variability on timescales of months to years (e.g., Lundgren et al. 2007; Gibson et al. 2008; Filiz et al. 2013; Grier et al. 2015; McGraw et al. 2017, 2018). This variability primarily manifests as changes in the depth of the trough with a few cases of velocity changes (e.g., Hamann et al. 1997; Vilkoviskij & Irwin 2001; Grier et al. 2016). Two supported possibilities to account for these depth changes are a change in the ionizing photon rate incident on the outflow (e.g., Arav et al. 2015; Grier et al. 2015; Wang et al. 2015; Wildy et al. 2015) or a change in the total hydrogen column density by material moving into the line of sight (e.g., Hamann et al. 2008; Hall et al. 2011; Vivek et al. 2012; Capellupo et al. 2013). Recent work by He et al. (2017) favors the former as the dominant cause for trough variability.

Table 1
HST/COS Observations from 2010 and 2017 for LBQS 1206+1052

	Date		
	2010 May 8	2017 Jul 18	2017 Jul 18
HST/COS Grating	G130M	G130M	G160M
Exposure Time (s)	4840	4320	4640
Observed Range (Å)	1150–1445	1150–1445	1400–1780
Rest-frame Range (Å)	825–1020	825–1020	1000–1275

LBQS 1206+1052 was reported in the Large Bright Quasar Survey catalog by Hewett et al. (1995). Later, Gibson et al. (2009) identified a Mg II ($\lambda\lambda$ 2796, 2803) trough in a Sloan Digital Sky Survey spectrum (data release 5), classifying it as a LoBAL quasar. Work by Ji et al. (2012) identified two outflows, v700 (centroid velocity ≈ -730 km s^{-1}) and v1400 (centroid velocity ≈ -1400 km s^{-1}), from Mg II and He I* absorption troughs. These outflows cover a velocity width of $\sim$2000 km s^{-1}. Chamberlain & Arav (2015) analyzed archival *HST*/COS spectra from 2010 and determined the distance of the v1400 outflow from the central source to be 840 pc. There was concern, however, that the absorption troughs used to calculate the density could have been saturated, which can lead to an overestimation of R, prompting the follow-up observations in this work.

Sun et al. (2017) presented a four-year (2012–2016) observing campaign of LBQS 1206+1052. Balmer absorption was identified for the v700 outflow, which yielded an estimate for the hydrogen number density in the range of 10^9–10^{10} cm^{-3} and a distance of $\sim$1 pc. Both the v1400 and v700 outflows showed absorption trough variability (only trough depth) consistent with the ionizing source changing.

In this paper, we present in Section 2 the new *Hubble Space Telescope* Cosmic Origins Spectrograph (*HST*/COS) observations of LBQS 1206+1052, which cover a larger wavelength range compared to the 2010 observations. We also discuss in Section 2 the spectral fitting for the continuum and emission lines. Section 3 details the extraction of ionic column densities, photoionization modeling, and density calculations of the new observations as well as from the 2010 data. Our results and discussion on the physical properties, distances, energetics, and variability of the outflows are in Section 4. A summary with conclusions is in Section 5. We adopt an $h = 0.7$, $\Omega_m = 0.3$, and $\Omega_\Lambda = 0.7$ cosmology throughout this paper (see, e.g., Bennett et al. 2014).

2. Observations, Data Reduction, and Spectral Fitting

LBQS 1206+1052 (J2000: R.A. = 12 09 24.079, decl. = +10 36 12.06, $z = 0.3955$) was first observed by *HST*/COS in 2010 May (PID 11698) and again in 2017 July (PID 14777). The details of each observation are given in Table 1. The new observations cover a larger wavelength range, allowing for more density-sensitive diagnostics to be observed. For consistency, the 2010 data was reprocessed in the same way as the 2017 data, using up-to-date calibration files for each observation. The 2010 data were obtained at COS detector lifetime position 1 (LP1), for which the wavelength calibration is described in Space Telescope Science Institute Newsletter (2016) and the flat-field derivation in Ely et al. (2011). The 2017 data were obtained at LP3, and we used updated wavelength calibrations that are not yet publicly available to

the science community. Flat fields appropriate to LP3 were derived at the new detector position using the methods described in Ely et al. (2011). The data was reduced with a modified version of the STScI CALCOS v3.2.1 pipeline software. This version estimates errors for each pixel by the expression

$$\mathrm{err}_i = \left(\frac{N}{(s_i t)^2} \right), \qquad (1)$$

where err_i is the error for pixel i, s_i is the sensitivity for pixel i, N is the gross counts, and t is the exposure time. Then, we binned each spectrum by 15 pixels and added the errors in quadrature. Finally, to render our Poisson-distributed errors as more similar to a Gaussian distribution, we added an additional count of flux to the errors, i.e.,

$$\mathrm{err}G_i = \mathrm{err}_i + (15 s_i t)^{-1}, \qquad (2)$$

where $\mathrm{err}G_i$ is the Gaussian distributed error for binned position i, and 15 is the bin size.

The final one-dimensional spectrum for the 2017 data is shown in Figure 1, while the spectrum for the 2010 data matches very well with Figure 11 of Sun et al. (2017). There is a gap in the G130M detector around 1300 Å. Absorption troughs from ions H I, C III, N III, N V, O VI, Si II, Si III, P V, S III, S IV, and S VI are identified for both outflows in Figure 1 as well. Following the methodology of Chamberlain & Arav (2015), we fit the unabsorbed continuum emission with a power law and any emission lines with Gaussian profiles. The emission lines typically have both broad and narrow components originating from two distinct regions. The power law is of the form $F(\lambda) = F_{1100}(\lambda/1100)^\alpha$, where $F_{1100} = 1.28 \times 10^{-15}$ erg s^{-1} cm^{-2} Å^{-1} and $\alpha = 2.4$. Since the absorption occurs on the blue side of the emission lines, the red side of each line was used to constrain the Gaussian fits. The centroid of each Gaussian was fixed at the rest-frame wavelength for each line, and lines originating from the same ions were modeled with the same FWHM. In the region where the power law did not match the spectrum (1500–1650 Å, observed frame), a cubic spline was used to correct the fit. The solid red contour in Figure 1 shows the full, unabsorbed emission model adopted in this work.

3. Data Analysis

3.1. Ionic Column Density

We measured the column density of a particular ion by using the apparent optical depth (AOD) method (Savage & Sembach 1991). This method assumes the outflow covers the source completely and homogeneously (i.e., the optical depth is the same across the source at each velocity). Therefore, for the optical depth,

$$\tau(\lambda) \equiv -\ln\left(\frac{F_{\mathrm{obs}}(\lambda)}{F_0(\lambda)} \right), \qquad (3)$$

where $F_{\mathrm{obs}}(\lambda)$ and $F_0(\lambda)$ are the observed flux and unabsorbed emission model flux, respectively. The ionic column density can then be solved from Equation (9) in Savage & Sembach (1991):

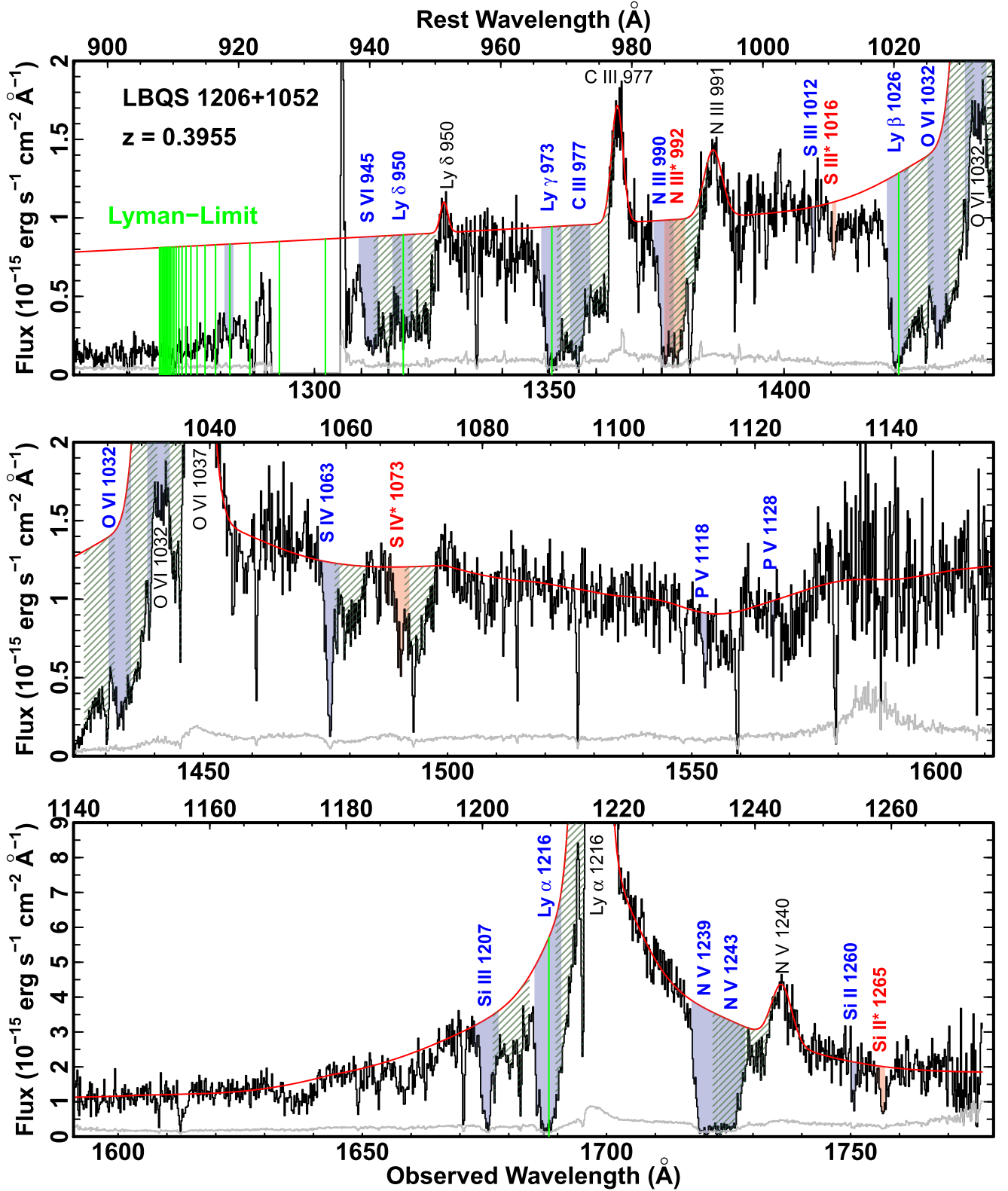$$N_{\mathrm{ion}} = \frac{m_e c}{\pi e^2 f \lambda} \int \tau(v) dv, \qquad (4)$$

Figure 1. Portion of the *HST*/COS 2017 spectrum (in black) showing the main absorption features. The blue and red shaded regions are the absorption trough transitions of the resonance and excited states, respectively, for the v1400 outflow. The slanted, dark green shaded regions show the absorption trough transitions for the v700 outflow. The red contour is the unabsorbed emission model and the green vertical lines indicate the Lyman series of hydrogen. The gray spectrum shows the errors, and emission lines are labeled in black.

where $N_{\rm ion}$ is the column density for an ionic transition, m_e is the mass of the electron, c is the speed of light, e is the electric charge, f is the oscillator strength for the ionic transition, λ is the wavelength of the ionic transition, and $\tau(v)$ is the optical depth as a function of velocity. A variation of Equation (4) is used by Chamberlain & Arav (2015) for blended troughs. AGN

outflow troughs have been shown to suffer from non-black saturation, where the trough is saturated but the flux does not reduce to zero (e.g., Arav et al. 2008; Borguet et al. 2012b, 2013). Typically, cases of non-black saturation are identified when measured optical depth ratios of two absorption lines from the same lower energy level deviate from the theoretical value determined by their oscillator strengths and wavelengths, i.e., $\frac{\tau_2}{\tau_1} \neq \frac{\lambda_2 f_2}{\lambda_1 f_1}$. In such cases, the AOD N_{ion} measurement is treated as a lower limit.

Figure 2 highlights the main troughs from the 2017 data, and the total ionic column density (excited plus resonance column densities) for each ion of the v1400 outflow is listed in Table 2. The predicted column densities from the best-fit model are also given (see Section 3.2 and Figure 3). The excited states for N III, S III, S IV, and Si II have multiple transitions. These transitions have small separations so we combine each set of transitions into a single transition as labeled in Figure 2. For the blended troughs of N III and S IV, we employed Equation (1) from Chamberlain & Arav (2015) to calculate the ionic column densities. The blue and red contours show the best component fits to each trough. The light green contour is the combination of the individual components for N III. As in Figure 1, the dark green, slanted lines show where the v700 absorption troughs should be located, contaminating each measurement. This contamination is minor in the case of S IV since the fitting effectively removes it, but is potentially quite significant for N III. However, as we will discuss later in Section 4, we believe the N III contamination is small and does not affect our results.

For all other troughs in Figures 1 and 2, we calculate the ionic column densities using Equation (4). The shaded blue and red regions show the integration range used for determining the ionic column densities of the resonance and excited state transitions, respectively. We estimate an upper limit for H I from the Lyman limit near 912.3 Å in the same way as Chamberlain & Arav (2015) with the expression $\tau = a_\nu N_H$, where a_ν is the photoionization cross section of H I. As stated before, non-black saturation is a concern. For H I, measurements closer to the Lyman limit are less saturated since the oscillator strength decreases. Therefore, the measurement at H I 923.2 Å is the largest lower limit we reliably measure. Considering the very low abundance of phosphorus ($\approx 10^{-3}$ times the abundance of carbon), we treat the P V column density as a measurement. The column densities of O VI and Si II are also taken as measurements for reasons discussed in Section 4. All other measurements are taken as lower limits. We calculated the ionic column densities from the 2010 spectra in the same way. Ar IV, like P V, has a small abundance ($\approx 10^{-2}$ times the abundance of carbon), and therefore is not likely saturated. In all measurements, the adopted values (see Table 2) assume errors of at least 20% to account for systematic uncertainties in the unabsorbed emission model. These systematic uncertainties arise from features like those seen in Figure 1 around the S IV absorption troughs, where shifting the continuum to better match those features results in total S IV column density errors near 20%.

3.2. Photoionization Modeling

The ionization structure of the outflow determines the ionic column densities we measure. Therefore, by using the ionic column densities in conjunction with a grid of Cloudy (Ferland et al. 2017; version c17.00) photoionization models, a solution for the hydrogen column density (N_H) and ionization parameter can be found. For each model, we assumed solar metallicity (Grevesse et al. 2010), the UV-soft SED (Dunn et al. 2010), and a stopping criterion that the proton to hydrogen density ratio equals 0.01 (ensuring a wide range of N_H). The UV-soft SED was chosen since the overall UV–optical spectrum shown in Figure 13 of Sun et al. (2017) resembles AGN SEDs illustrated in Shang et al. (2005, 2011), which are similar to the UV-soft SED. In this section, we do not take into account the effects the v700 outflow has on the SED before reaching the v1400 outflow (see Sun et al. 2017; their "shading effect"). This is because the properties of the v700 outflow have not been determined robustly since the Balmer, He I*, and Mg II absorption troughs were not covered in the 2017 epoch. However, in Section 4.5, we show that when the v700 properties from Sun et al. (2017) are assumed, the distance, mass flux, and kinetic luminosity for the v1400 outflow are only mildly affected by this "shading effect."

For a particular pair of N_H and U_H, ionic column densities from the model are compared to the measured counterparts. In Figure 3, the colored contours for individual ions show where the model predicted ionic column densities are consistent ($<1\sigma$) with the observed values. The colored contours with solid, dotted, or dashed lines show the ionic column densities treated as measurements, upper limits, or lower limits, respectively. The best-fit solution is determined through χ^2-minimization of the model predicted ionic column densities compared to the measured, ionic column densities (all values in Table 2). The solutions and corresponding 1σ uncertainties are the black symbols and ellipses, respectively.

3.3. Electron Number Density

The energy levels for the excited states of S IV, S III, Si II, and N III are populated by collisional excitations with free electrons. Therefore, the relative populations between the excited and resonance states depend on the electron number density, n_e. There is a small temperature dependence, but the range in temperatures allowed by the best-fit photoionization solution is less than 1000 K (introducing only a few percent error in n_e). Following the methodology of previous works (e.g., Korista et al. 2008; Borguet et al. 2012a; Arav et al. 2013, 2018; Chamberlain & Arav 2015), we used the CHIANTI 8.0.7 database (Dere et al. 1997; Landi et al. 2013) to calculate the predicted population ratios of the excited to resonance states for each ion. This ratio is equal to the ratio of the column densities of the excited to resonance states. The N_{ion} measured values are given in Table 3.

In the top panel of Figure 4, the colored, dashed contours show the expected column density ratio as a function of electron number density for each ion at the temperature of the 2017 photoionization solution, 13,200 K. Overlaid on the contours are the measured column density ratios and uncertainties of each ion from the 2017 data (Table 3). As can be seen, the column density ratios for N III and S III are consistent with 1, indicative of saturation (Borguet et al. 2013; Arav et al. 2018). This means the value of the true ratio could be greater than or less than 1, depending on if the excited or resonance trough is more heavily saturated (Arav et al. 2018). The model predicted total column densities for N III and S III in Table 2 supports the saturation claim since they are 2–3 times larger than each respective measured value. Also, the upper error for the Si II column density ratio is large enough that the
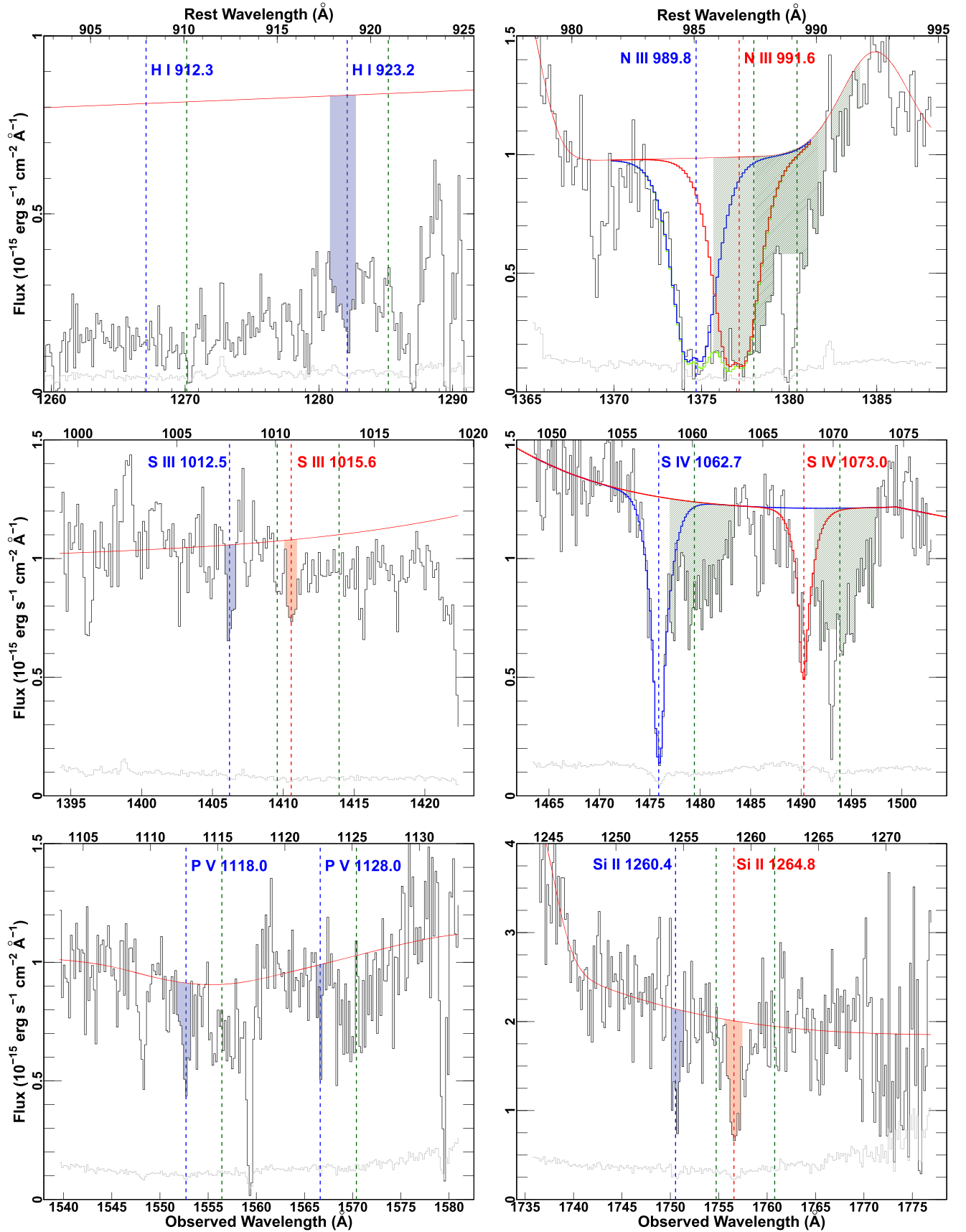
Figure 2. Zoomed-in portions of Figure 1 (same shaded regions and error spectrum). Overlaid on the N III and S IV troughs are blue and red contours that are the components for the best-fit model of the v1400 outflow for each trough. For N III, the combination of the components is shown as a light green contour. The blue and red labels and similarly colored vertical, dashed lines identify the resonance and excited line transitions, respectively, of each ion. The vertical, green dashed lines show the v700 outflow counterparts to the v1400 outflow line transitions.

Table 2
Total Ionic Column Densities in Component v1400

Ion	Measured (10^{13}cm^{-2})	Adopted (10^{13}cm^{-2})	Best Model (10^{13}cm^{-2})
	2017 Data		
H I Upper Limit	$28,000^{+2800}_{-2800}$	$28,000^{+5600}$	33,000
H I Lower Limit	$12,000^{+690}_{-530}$	$12,000_{-2400}$	33,000
N III	710^{+60}_{-60}	710_{-140}	2550
N V	510^{+55}_{-20}	510_{-100}	740
C III	82^{+5}_{-3}	82_{-16}	10,800
O III	1400^{+310}_{-160}	1400_{-280}	31,500
O VI	430^{+8}_{-7}	430^{+430}_{-86}	1070
Si II	$9.0^{+1}_{-0.8}$	$9.0^{+1.8}_{-1.8}$	8.1
Si III	$18^{+1.0}_{-0.7}$	$18_{-3.6}$	230
P V	$8.2^{+1.4}_{-1.1}$	$8.2^{+1.6}_{-1.6}$	6
S III	97^{+9}_{-8}	97_{-19}	200
S IV	630^{+60}_{-60}	630_{-130}	610
S VI	230^{+11}_{-8}	230_{-47}	230
	2010 Data		
H I Upper Limit	$25,000^{+830}_{-790}$	$25,000^{+5000}$	26,500
H I Lower Limit	$16,000^{+1100}_{-860}$	$16,000_{-3200}$	26,500
N III	690^{+31}_{-31}	690_{-140}	2080
C III	93^{+6}_{-3}	93_{-19}	8810
O III	1700^{+320}_{-130}	1700_{-340}	24,700
O VI	410^{+15}_{-11}	410^{+410}_{-82}	940
S III	89^{+16}_{-13}	89_{-18}	160
S VI	210^{+9}_{-7}	210_{-42}	200
Ar IV	160^{+94}_{-42}	160^{+94}_{-42}	120

Note. Total ionic column densities (excited plus resonance, where applicable, of the v1400 outflow) for each observation with the measured and adopted errors. The predicted column densities from the best-fit Cloudy model are in the last column. Since the flux decreased from 2010 to 2017, Ar IV was not reliably measured for the 2017 data.

ratio is consistent with the asymptotic maximum value. Therefore, the only reliable measurement of the electron number density is from the S IV column density ratio, which is firmly below 1. We calculate a value for the electron number density of $\log(n_e) = 4.23^{+0.09}_{-0.09}$ cm^{-3} based on the S IV column density ratio and treat the measurements from the other column density ratios as lower limits.

4. Results and Discussion

4.1. v1400 Outflow Properties, Distance, and Energetics

Using the methodology of Borguet et al. (2013), we determine the distance from the central source to the v1400 outflow from the ionization parameter:

$$U_H = \frac{Q_H}{4\pi R^2 n_H c}, \quad (5)$$

where R is the distance from the central source, n_H is the hydrogen number density ($n_e = 1.2 n_H$ for highly ionized plasma), c is the speed of light, and Q_H is the ionizing hydrogen photon rate. We calculate Q_H by integrating the UV-soft SED, normalized to each epoch, for energies above 1 Ryd. Sun et al. (2017) showed that the UV portion of the spectrum is likely heavily dust extincted. We concur with this
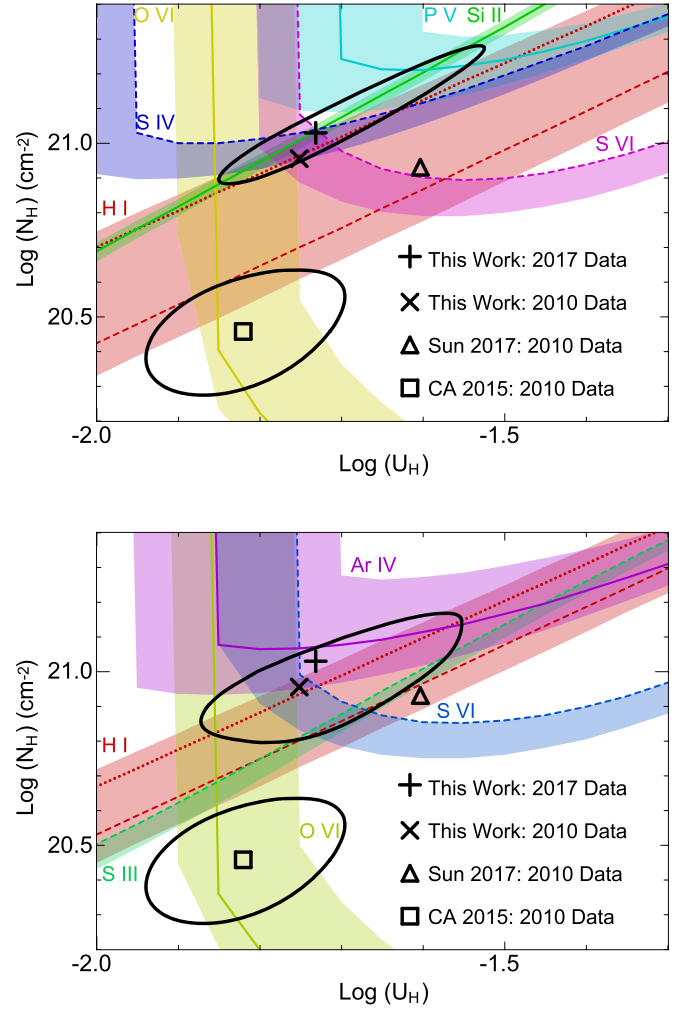

Figure 3. Top: photoionization solution for the v1400 outflow based on the 2017 data. Bottom: photoionization solution for the v1400 outflow based on the reprocessed 2010 data. For both panels: the colored contours show the model parameters that are consistent with the observed value. Solid, dotted, and dashed contours represent ionic column densities taken as measurements, upper limits, and lower limits, respectively. The shaded bands are the 1σ uncertainties for each contour (see Table 2). The solutions from Chamberlain & Arav (2015; CA 2015) and Sun et al. (2017; Sun 2017) are also shown. The plus, cross, triangle, and square symbols are the best χ^2-minimization solutions and the black ellipses (not available for Sun 2017) encircling them are their 1σ uncertainties.

Table 3
Excited and Resonance Ionic Column Densities

Column Density $(10^{13} \text{ cm}^{-2})$	v1400 2017 Data	v700 2017 Data	v1400 2010 Data
$N(\text{S IV}^*)$	200^{+21}_{-21}	400^{+24}_{-21}	...
$N(\text{S IV})$	430^{+50}_{-50}	250^{+17}_{-15}	...
$N(\text{Si II}^*)$	$5.8^{+0.9}_{-0.7}$	...	...
$N(\text{Si II})$	$3.3^{+0.5}_{-0.5}$	...	...
$N(\text{S III}^*)$	52^{+6}_{-5}	...	52^{+11}_{-9}
$N(\text{S III})$	45^{+7}_{-6}	...	55^{+11}_{-9}
$N(\text{N III}^*)$	370^{+30}_{-30}	...	360^{+24}_{-24}
$N(\text{N III})$	340^{+50}_{-50}	...	330^{+20}_{-20}

Note. Excited and resonance ionic column densities of the density-sensitive ions for the v1400 and v700 outflows in LBQS 1206+1052.
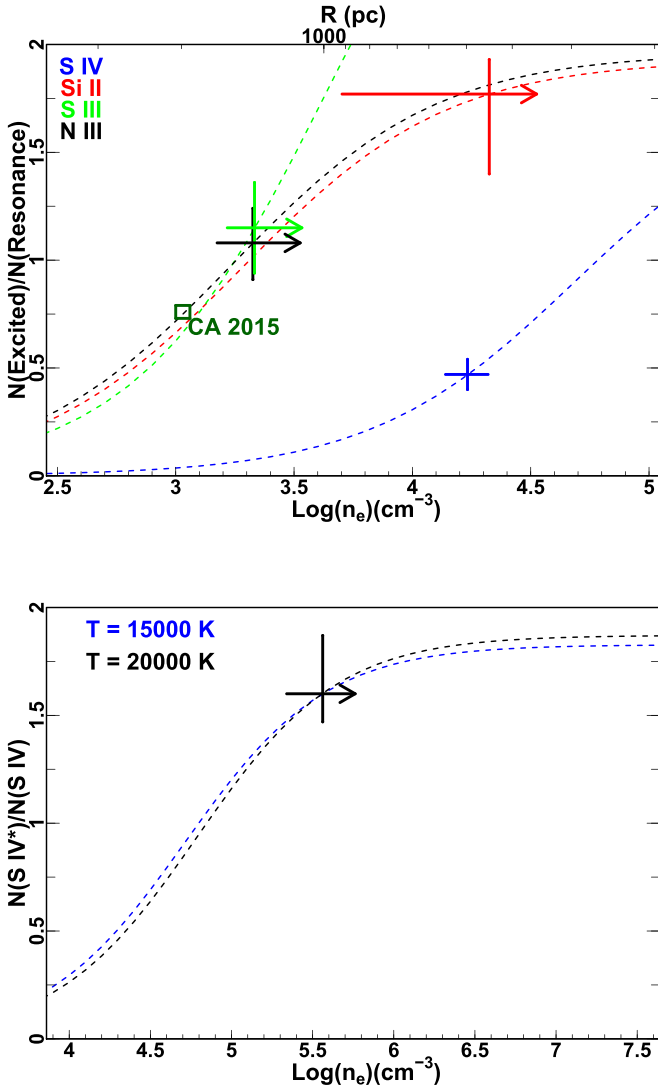
Table 4
Comparison: Physical Properties, Distances, and Energetics
of the v1400 Component

Analysis Data	TW 2017	TW 2010	CA 2010	Sun 2010
$\log(N_H)$ [cm^{-2}]	$21.03^{+0.25}_{-0.15}$	$20.96^{+0.21}_{-0.16}$	$20.46^{+0.17}_{-0.17}$	20.93
$\log(U_H)$ [dex]	$-1.73^{+0.21}_{-0.12}$	$-1.75^{+0.20}_{-0.12}$	$-1.82^{+0.12}_{-0.12}$	-1.60
$\log(n_e)$ [cm^{-3}]	$4.23^{+0.09}_{-0.09}$	$\cdots$	$3.03^{+0.06}_{-0.06}$	3.08
Distance [pc]	500^{+100}_{-110}	[a]590^{+120}_{-130}	840^{+60}_{-60}	2800
$\dot{M}$ [$M_\odot$ yr^{-1}]	$8.9^{+7.2}_{-3.1}$	[a]$8.8^{+5.8}_{-3.2}$	$9.0^{+3.0}_{-3.0}$	40
$\log(\dot{E}_K)$ [erg s^{-1}]	$42.8^{+0.26}_{-0.19}$	[a]$42.8^{+0.22}_{-0.20}$	$42.8^{+0.15}_{-0.15}$	43.4

Notes. Comparison between this work (TW), Chamberlain & Arav (2015; CA), and Sun et al. (2017; Sun), of the physical properties, distances, and energetics of the v1400 outflow in LBQS 1206+1052.
[a] Assumes the 2017 data n_e measurement.

Figure 4. Top: electron number density, n_e, and distance from the central source, R (Equation (5)), of the v1400 outflow based on the 2017 data column density ratios of S IV, Si II, S III, and N III. The dashed contours are the expected ratios for each ion at a given density for a temperature of 13,500 K, the average temperature from the photoionization solution. The arrows indicate lower limits. The solution for N III from Chamberlain & Arav (2015) is also shown. Bottom: the lower limit to the electron number density for the v700 outflow based on the S IV ratio. The dashed contours show the expected ratio for a given density for two temperatures, encompassing the average temperatures based on the photoionization solutions of Sun et al. (2017). This lower limit is consistent with the Sun et al. (2017) range: $n_e = 10^9$–10^{10} cm^{-3}.

assessment (see Section 4.2). Therefore, we chose to scale the UV-soft SED for the 2010 data to the same normalization as Sun et al. (2017), $L_{3000} = 4.7 \times 10^{45}$ erg s^{-1}. For the 2017 data, we scaled the normalization by the amount the continuum level decreased between the 2010 and 2017 epochs ($\sim$20%). This yields $Q_H = 2.45 \times 10^{56}$ s^{-1} and $Q_H = 3.09 \times 10^{56}$ s^{-1} for the 2017 data and 2010 data, respectively. Following the assumptions of Borguet et al. (2012b), the mass flow rate and kinetic luminosity are given by the following expressions:

$$\dot{M} \simeq 4\pi\Omega R N_H \mu m_p v, \qquad (6)$$

$$\dot{E}_K \simeq \frac{1}{2}\dot{M}v^2, \qquad (7)$$

where the global covering factor $\Omega = 0.08$ (fraction of outflows with S IV/S IV* troughs; Borguet et al. 2013), R is the distance from the central source, $\mu = 1.4$ is the mean atomic mass per proton, N_H is the hydrogen column density, m_p is the proton mass, and v is the outflow velocity.

Table 4 contains the physical properties, energetics, and distances for the v1400 outflow as determined by this work, Chamberlain & Arav (2015), and Sun et al. (2017). Since the column density ratios and total column densities (see Tables 2 and 3) of N III and S III indicate saturation, and they were unaware of the dust extinction, the results from Chamberlain & Arav (2015) differ significantly from ours. However, their main conclusion that this outflow is not a major contributor to AGN feedback still holds. The main difference between our work and Sun et al. (2017), besides the number density, is the choice of SED. Sun et al. (2017) employed the MF87 SED (Mathews & Ferland 1987), which is harder in the UV compared to the UV-soft SED. Choosing the MF87 SED results in a Q_H over two times larger than ours, which when combined with the different electron densities, gives the much larger distance they calculate.

4.2. Internal Dust Extinction

As stated in Section 4.1, Sun et al. (2017) provided evidence that heavy dust extinction is present in the 2010 data. They noted that the emission line profiles of C III λ977, N III λ992, and O VI λ1031 had components too wide to be from the narrow emission line region (typical FWHM $\sim$500 km s^{-1}) and too narrow to be from the broad emission line region. This type of situation can occur when the broad emission lines are suppressed by dust extinction from the torus and intermediate-width emission lines from the inner face of the torus begin to dominate the observed emission line profiles (see, e.g., Li et al. 2015).
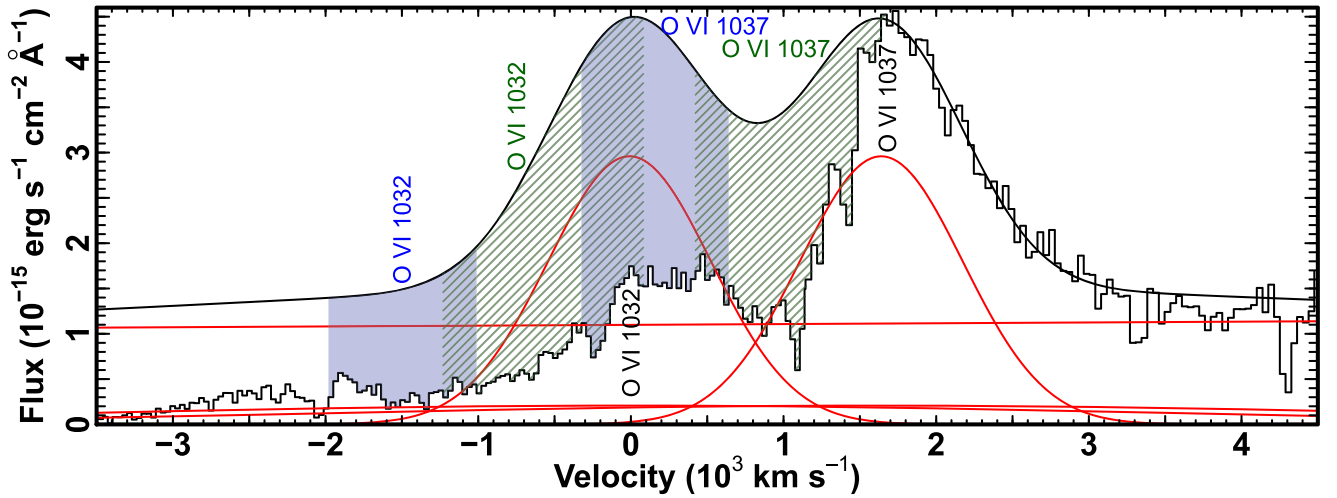
Figure 5. Spectrum, unabsorbed emission model, and O VI absorption troughs centered around the O VI emission lines. In red are the unabsorbed emission model components of the power law with two broad and two intermediate-width Gaussian profiles.

Similar intermediate-width emission lines are still seen in the 2017 data. The fits to the emission lines of Ly $\lambda1216$, O VI $\lambda1032$, and O VI $\lambda1037$ in the unabsorbed emission model of Figure 1 comprise one weak but broad ($\sim$20% of max height, FWHM $\sim$6000 km s^{-1} with errors <20%) and one strong yet still wide ($\sim$80% of max height, FWHM $\sim$1000 km s^{-1} with errors <15%) Gaussian components. The former component is wide enough to be originating from the broad emission line region, but the latter component is too wide to be coming from the narrow emission line region. The fits to the C III $\lambda977$ and N III $\lambda992$ emission lines also only require a single Gaussian component with an FWHM $\sim$1000 km s^{-1} (with errors <20%). The persistence of these intermediate-width emission lines and disappearance of the broad-line components blueward of O VI $\lambda1032$ lead us to believe there is heavy dust extinction in the UV spectrum.

4.3. Photoionization Variability

In Section 1, we mentioned two possible causes of variability for outflow absorption troughs seen in quasar spectra, a change in ionizing flux or material moving into the line of sight, and that Sun et al. (2017) supported the former. As can be seen in Figure 3, the 2010 and 2017 photoionization solutions are compatible with either cause. However, given the arguments of Sun et al. (2017) that the absorption trough depths both increased and decreased over time while the velocity remained constant, gas clouds moving into and out of the line of sight with the same velocity is highly unlikely. Therefore, a change in ionizing flux is the likely cause for the trough depth variability.

One concern Sun et al. (2017) had was the timescale needed for the outflow to respond was too long ($\sim$20 years). However, with the larger density determined in this work, the timescale is over a factor of 10 shorter when the same expression from Sun et al. (2017), $t = (\alpha_i n_e)^{-1}$, is used. Thus, the outflow response is quick enough for the optical depth changes seen in Sun et al. (2017).

4.4. Saturation and Contamination

As stated in Section 3.1, the column densities of Si II and O VI were taken as measurements. Since the Si II column density ratio ($1.76^{+0.43}_{-0.30}$) is close to the maximum value physically allowed ($\sim$2), we believe the Si II column density is not significantly saturated, if at all. Sun et al. (2017) argued that the v1400 O VI $\lambda1032$ trough is saturated. They explained the residual intensity of this trough as an intermediate-width emission line that is not covered by the v1400 outflow. However, the 2017 data cover the O VI $\lambda1037$ emission for the first time, providing new constraints. Figure 5 shows the spectrum, unabsorbed emission model, and O VI absorption troughs centered around the O VI emission lines as well as the decomposition of the unabsorbed emission model (a power law with two broad and two intermediate-width Gaussian profiles all in red). This model is minimalistic in that the peak of the O VI $\lambda1037$ emission line is assumed to be the maximum and the O VI $\lambda1032$ emission line is equal in strength. The O VI $\lambda1032$ emission can be up to a factor of two higher (the oscillator strengths for these lines differ by this same factor) but cannot be weaker.

Given the minimalistic model, the v1400 outflow must cover all components of the unabsorbed emission model, or else the residual intensity should trace the Gaussian profile for the O VI $\lambda1032$ emission line. Therefore, the residual intensity is not from an uncovered emission region, as was previously thought by Sun et al. (2017). Since the column density measurement for the v1400 O VI $\lambda1032$ is less model dependent than the corresponding v1400 O VI $\lambda1037$, we adopted its value and gave a conservative upper error of a factor of two to account for any saturation that may be present.

The contamination in the v1400 N III troughs by the v700 N III troughs affects the v1400 N III column density ratio (see Figure 2). If the contamination is large enough, the v1400 N III column density ratio could fall sufficiently below 1 that there would be a discrepancy between the value for the electron number density for the v1400 outflow as determined by the N III and S IV column density ratios.

To estimate the amount of contamination, a constraint on the v700 N III column density ratio is needed. From Sun et al. (2017), the hydrogen density, n_H, was estimated for the v700 outflow to be in the range of 10^9–10^{10} cm^{-3}. To corroborate this result, we calculated the S IV column density ratio (Table 3) for the v700 outflow from the associated regions in Figure 2. As can be seen in the lower half of Figure 4, we

derived a lower limit on the electron number density of $\log(n_e) > 5.34$ cm^{-3} from the measured ratio and temperature range from the photoionization solutions in Sun et al. (2017) for the v700 outflow. Furthermore, we tested their best-fit model by measuring the column density of P V $\lambda 1118$ for the v700 outflow, a value of $17^{+3}_{-3} \times 10^{13}$ cm^{-2}, and found it to be consistent with the 16×10^{13} cm^{-2} value predicted by the best-fit model. Therefore, the density range is sound, and the N III column density ratio for the v700 outflow must be in the range of 1–2, depending on the saturation.

The most contamination that can occur is when the ratio is 1, maximizing the v700 N III resonance column density, which affects the value of the v1400 N III excited column density. To estimate the v700 N III column density for the resonance transition, we calculated the column density for the right half of the v700 N III excited transition (between 989 Å and 992 Å, rest frame; Figure 2), which suffers the least contamination from other troughs, and doubled it. This yielded a value of 90×10^{13} cm^{-2}. Assuming this only affects the N III excited column density of the v1400 outflow (it would affect both) and ignoring saturation in the v1400 N III troughs, the v1400 N III column density ratio only decreases to $0.82^{+0.17}_{-0.17}$, remaining consistent with a value of 1.

4.5. v700 Outflow "Shading Effect" on the v1400 Outflow

To test the effects the v700 "shading" has on the v1400 outflow, we first used the best-fit parameters of Sun et al. (2017) for the v700 outflow and generated a Cloudy model, assuming the UVsoft SED. From this model, we used the transmitted SED as the input SED to generate a new grid of models to find a new photoionization solution for the v1400 outflow. The original UVsoft SED and shaded SED can be seen in the top panel of Figure 6. The major difference is the decrease in photons between 4 and 100 Rydbergs. This decrease in photons affects the ionization parameter required to match the column densities of high-ionization ions like O VI as seen in the bottom panel of Figure 6. The O VI contour has shifted by ~ 0.7 dex in ionization parameter. This shift necessitates a two-phase photoionization solution to satisfy the observed ionic column densities: one component with $\log(N_H) = 20.90^{+0.26}_{-0.35}$ cm^{-2} and $\log(U_H) = -1.72^{+0.17}_{-0.20}$; and a second component with $\log(N_H) = 20.92^{+0.33}_{-0.34}$ cm^{-2} and $\log(U_H) = -1.07^{+0.33}_{-0.12}$. A single-phase photoionization solution cannot satisfy the ionic column densities of Si II and O VI simultaneously without overpredicting the P V column density by an order of magnitude.

The lower-ionization parameter solution contains nearly all of the S IV column density, and therefore corresponds to the same density as in the unshaded solution. This allows for the distance to be determined. Using the same normalization as in Section 4.1 and the shaded SED, we calculate $Q_H = 1.72 \times 10^{56}$ s^{-1} and $R = 420^{+130}_{-80}$ pc. This yields a mass flux and kinetic luminosity of $\dot{M} = 11.3^{+8.1}_{-5.5}$ and $\log(\dot{E}_K) = 42.9^{+0.23}_{-0.29}$ erg s^{-1}, respectively. This distance, mass flux, and kinetic luminosity are all consistent with the values determined for the unshaded photoionization solution. The main difference is that the shaded solution requires a two-phase ionization outflow with $\Delta U \approx 0.7$.
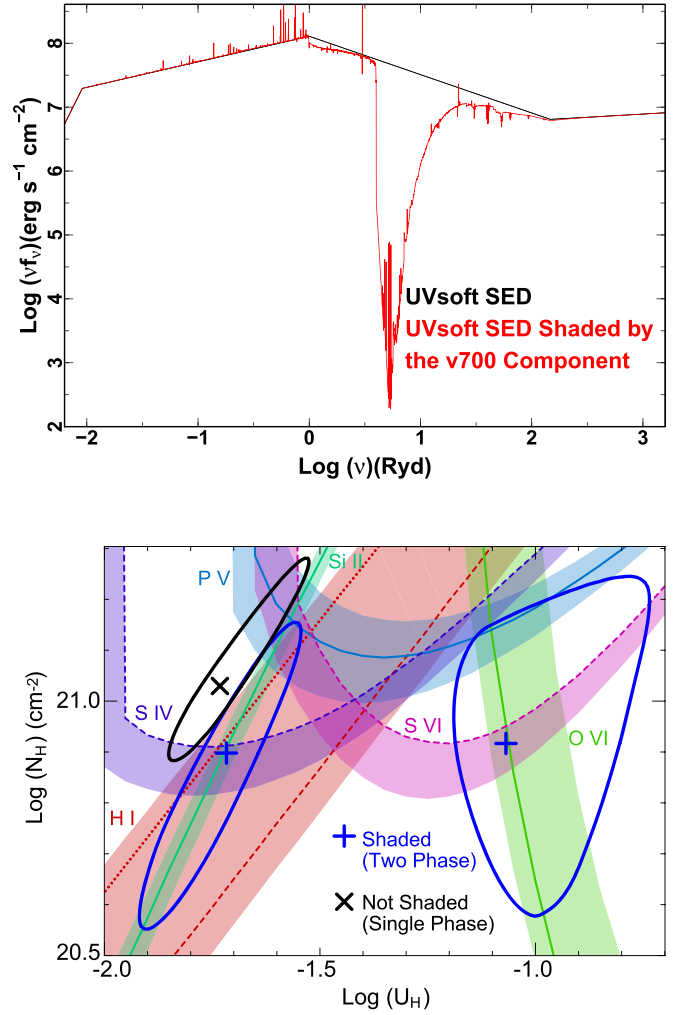

Figure 6. Top: comparison between the UVsoft SED and the transmitted SED after being shaded by the v700 outflow. Bottom: two-phase photoionization solution for the v1400 outflow assuming the transmitted SED. The colored contours, shaded bands, symbols, and ellipses have the same meanings as in Figure 3.

5. Summary and Conclusions

In this paper, we presented new *HST*/COS spectra for the quasar outflows seen in LBQS 1206+1052. We identified absorption troughs in this spectra from ions H I, C III, N III, N V, O III, O VI, S III, S IV, S VI, Si II, Si III, and P V. Then, we calculated ionic column densities for the v1400 outflow from these data as well as reprocessed, archival *HST*/COS data (Table 2). From these ionic column densities and a grid of photoionization models, we determined the best-fit ionization parameter and hydrogen column density for each data set: $\log(U_H) = -1.75^{+0.20}_{-0.12}$ and $\log(N_H) = 20.96^{+0.21}_{-0.16}$ cm^{-2} for the 2010 data and $\log(U_H) = -1.73^{+0.21}_{-0.12}$ and $\log(N_H) = 21.03^{+0.25}_{-0.15}$ cm^{-2} for the 2017 data.

For the ions S IV, Si II, S III, and N III, we detected troughs from both resonance and excited states, the ratios of which are density sensitive. These ratios were compared to theoretical models of the ratio versus electron number density. The S IV column density ratio provided the adopted electron number density, $\log(n_e) = 4.23^{+0.09}_{-0.09}$ cm^{-3}. The column density ratios from N III and S III were consistent with a value of 1, indicative of saturation, and therefore only gave lower limits to n_e. The electron number

density determined from the Si II column density ratio was also taken as a lower limit since the upper limit of the ratio was consistent with n_e being much larger than the critical density. From the adopted electron number density, the distance of the v1400 outflow from the central source was calculated with Equation (5), yielding $R = 500^{+100}_{-110}$ pc. Using this distance and Equations (6) and (7), the mass flux and kinetic luminosity were also determined to be $\dot{M} = 8.9^{+7.2}_{-3.1}\, M_\odot\, \mathrm{yr}^{-1}$ and $\log(\dot{E}_K) = 42.8^{+0.26}_{-0.19}\, \mathrm{erg\, s}^{-1}$, respectively.

The following conclusions emerge from this work:

1. The new observations, with the wider wavelength coverage, were paramount in determining that the correct electron number density for the v1400 outflow in LBQS 1206+1052 is over an order of magnitude larger than previously thought. This coupled with accounting for dust extinction decreased the distance by nearly a factor of two.

2. Using a shaded SED leads to a two-phase outflow for the v1400 component but has little effect on R, $\dot{M}$, and $\dot{E}_K$.

3. For the v700 outflow, using the S IV ratio, we set a lower limit on the electron number density that is consistent with previous results.

ORCID iDs

Timothy R. Miller ⓘ https://orcid.org/0000-0002-0730-2322
Xinfeng Xu ⓘ https://orcid.org/0000-0002-9217-7051
Gerard A. Kriss ⓘ https://orcid.org/0000-0002-2180-8266
Guilin Liu ⓘ https://orcid.org/0000-0003-2390-7927

References

Aldcroft, T. L., Bechtold, J., & Elvis, M. 1994, ApJS, 93, 1
Anglés-Alcázar, D., Davé, R., Faucher-Giguère, C.-A., Özel, F., & Hopkins, P. F. 2017, MNRAS, 464, 2840
Aoki, K., Oyabu, S., Dunn, J. P., et al. 2011, PASJ, 63, 457
Arav, N., Borguet, B., Chamberlain, C., Edmonds, D., & Danforth, C. 2013, MNRAS, 436, 3286
Arav, N., Chamberlain, C., Kriss, G. A., et al. 2015, A&A, 577, A37
Arav, N., Edmonds, D., Borguet, B., et al. 2012, A&A, 544, A33
Arav, N., Liu, G., Xu, X., et al. 2018, ApJ, 857, 60
Arav, N., Moe, M., Costantini, E., et al. 2008, ApJ, 681, 954
Barai, P., Proga, D., & Nagamine, K. 2011, MNRAS, 418, 591
Bautista, M. A., Dunn, J. P., Arav, N., et al. 2010, ApJ, 713, 25
Bennett, C. L., Larson, D., Weiland, J. L., & Hinshaw, G. 2014, ApJ, 794, 135
Blandford, R. D., & Begelman, M. C. 2004, MNRAS, 349, 68
Booth, C. M., & Schaye, J. 2009, in AIP Conf. Ser. 1201, The Monster's Fiery Breath: Feedback in Galaxies, Groups, and Clusters, ed. S. Heinz & E. Wilcots (Melville, NY: AIP), 21
Borguet, B. C. J., Arav, N., Edmonds, D., Chamberlain, C., & Benn, C. 2013, ApJ, 762, 49
Borguet, B. C. J., Edmonds, D., Arav, N., Benn, C., & Chamberlain, C. 2012a, ApJ, 758, 69
Borguet, B. C. J., Edmonds, D., Arav, N., Dunn, J., & Kriss, G. A. 2012b, ApJ, 751, 107
Capellupo, D. M., Hamann, F., Shields, J. C., Halpern, J. P., & Barlow, T. A. 2013, MNRAS, 429, 1872
Chamberlain, C., & Arav, N. 2015, MNRAS, 454, 675
Chamberlain, C., Arav, N., & Benn, C. 2015, MNRAS, 450, 1085
Choi, E., Ostriker, J. P., Naab, T., et al. 2017, ApJ, 844, 31
Ciotti, L., Ostriker, J. P., & Proga, D. 2009, ApJ, 699, 89
Dai, X., Shankar, F., & Sivakoff, G. R. 2008, ApJ, 672, 108
de Kool, M., Arav, N., Becker, R. H., et al. 2001, ApJ, 548, 609
de Kool, M., Becker, R. H., Arav, N., Gregg, M. D., & White, R. L. 2002, ApJ, 570, 514
Dere, K. P., Landi, E., Mason, H. E., Monsignori Fossi, B. C., & Young, P. R. 1997, A&AS, 125, 149
Dubois, Y., Volonteri, M., & Silk, J. 2014, MNRAS, 440, 1590
Dunn, J. P., Bautista, M., Arav, N., et al. 2010, ApJ, 709, 611
Edmonds, D., Borguet, B., Arav, N., et al. 2011, ApJ, 739, 7
Ely, J., Massa, D., Ake, T., et al. 2011, COS FUV Gridwire Flat Field Template, Instrument Science Report COS 2011-03 (Baltimore, MD: STScI), http://www.stsci.edu/hst/cos/documents/isrs/
Ferland, G. J., Chatzikos, M., Guzmán, F., et al. 2017, RMxAA, 53, 385
Filiz Ak, N., Brandt, W. N., Hall, P. B., et al. 2013, ApJ, 777, 168
Finn, C. W., Morris, S. L., Crighton, N. H. M., et al. 2014, MNRAS, 440, 3317
Gabel, J. R., Kraemer, S. B., Crenshaw, D. M., et al. 2005, ApJ, 631, 741
Gibson, R. R., Brandt, W. N., Schneider, D. P., & Gallagher, S. C. 2008, ApJ, 675, 985
Gibson, R. R., Jiang, L., Brandt, W. N., et al. 2009, ApJ, 692, 758
Grevesse, N., Asplund, M., Sauval, A. J., & Scott, P. 2010, Ap&SS, 328, 179
Grier, C. J., Brandt, W. N., Hall, P. B., et al. 2016, ApJ, 824, 130
Grier, C. J., Hall, P. B., Brandt, W. N., et al. 2015, ApJ, 806, 111
Hall, P. B., Anosov, K., White, R. L., et al. 2011, MNRAS, 411, 2653
Hamann, F., Barlow, T., Cohen, R. D., Junkkarinen, V., & Burbidge, E. M. 1997, in ASP Conf. Ser. 128, Mass Ejection from Active Galactic Nuclei, ed. N. Aravm, I. Shlosman, & R. J. Weymann (San Francisco, CA: ASP), 19
Hamann, F., Kaplan, K. F., Rodríguez Hidalgo, P., Prochaska, J. X., & Herbert-Fort, S. 2008, MNRAS, 391, L39
Hamann, F., & Sabra, B. 2004, in ASP Conf. Ser. 311, AGN Physics with the Sloan Digital Sky Survey, ed. G. T. Richards & P. B. Hall (San Francisco, CA: ASP), 203
Hamann, F. W., Barlow, T. A., Chaffee, F. C., Foltz, C. B., & Weymann, R. J. 2001, ApJ, 550, 142
He, Z., Wang, T., Zhou, H., et al. 2017, ApJS, 229, 22
Hewett, P. C., & Foltz, C. B. 2003, AJ, 125, 1784
Hewett, P. C., Foltz, C. B., & Chaffee, F. H. 1995, AJ, 109, 1498
Hopkins, P. F., Murray, N., & Thompson, T. A. 2009, MNRAS, 398, 303
Ji, T., Wang, T.-G., Zhou, H.-Y., & Wang, H.-Y. 2012, RAA, 12, 369
Khalatyan, A., Cattaneo, A., Schramm, M., et al. 2008, MNRAS, 387, 13
Knigge, C., Scaringi, S., Goad, M. R., & Cottis, C. E. 2008, MNRAS, 386, 1426
Korista, K. T., Bautista, M. A., Arav, N., et al. 2008, ApJ, 688, 108
Landi, E., Young, P. R., Dere, K. P., Del Zanna, G., & Mason, H. E. 2013, ApJ, 763, 86
Li, Z., Zhou, H., Hao, L., et al. 2015, ApJ, 812, 99
Lucy, A. B., Leighly, K. M., Terndrup, D. M., Dietrich, M., & Gallagher, S. C. 2014, ApJ, 783, 58
Lundgren, B. F., Wilhite, B. C., Brunner, R. J., et al. 2007, ApJ, 656, 73
Mathews, W. G., & Ferland, G. J. 1987, ApJ, 323, 456
McGraw, S. M., Brandt, W. N., Grier, C. J., et al. 2017, MNRAS, 469, 3163
McGraw, S. M., Shields, J. C., Hamann, F. W., Capellupo, D. M., & Herbst, H. 2018, MNRAS, 475, 585
Moe, M., Arav, N., Bautista, M. A., & Korista, K. T. 2009, ApJ, 706, 525
Murray, N., Chiang, J., Grossman, S. A., & Voit, G. M. 1995, ApJ, 451, 498
Peirani, S., Dubois, Y., Volonteri, M., et al. 2017, MNRAS, 472, 2153
Proga, D., & Kallman, T. R. 2004, ApJ, 616, 688
Proga, D., Stone, J. M., & Kallman, T. R. 2000, ApJ, 543, 686
Reichard, T. A., Richards, G. T., Hall, P. B., et al. 2003, AJ, 126, 2594
Rosas-Guevara, Y. M., Bower, R. G., Schaye, J., et al. 2015, MNRAS, 454, 1038
Savage, B. D., & Sembach, K. R. 1991, ApJ, 379, 245
Scannapieco, E., & Oh, S. P. 2004, ApJ, 608, 62

Schaye, J., Crain, R. A., Bower, R. G., et al. 2015, MNRAS, 446, 521
Shang, Z., Brotherton, M. S., Green, R. F., et al. 2005, ApJ, 619, 41
Shang, Z., Brotherton, M. S., Wills, B. J., et al. 2011, ApJS, 196, 2
Silk, J., & Rees, M. J. 1998, A&A, 331, L1
Space Telescope Science Institute Newsletter 2016, Hubble Space Telescope
    Updated COS/FUV Wavelength Dispersion Solution Reference File
    (DISPTAB) Released (Baltimore, MD: STScI), http://www.stsci.edu/
    hst/cos/documents/newsletters/cos_newsletters/full_stories/2016_05/
    new_disptab
Sun, L., Zhou, H., Ji, T., et al. 2017, ApJ, 838, 88
Taylor, P., & Kobayashi, C. 2015, MNRAS, 452, L59
Tornatore, L., Borgani, S., Viel, M., & Springel, V. 2010, MNRAS, 402, 1911

Trump, J. R., Hall, P. B., Reichard, T. A., et al. 2006, ApJS, 165, 1
Vestergaard, M. 2003, ApJ, 599, 116
Vilkoviskij, E. Y., & Irwin, M. J. 2001, MNRAS, 321, 4
Vivek, M., Srianand, R., Mahabal, A., & Kuriakose, V. C. 2012, MNRAS,
    421, L107
Volonteri, M., Dubois, Y., Pichon, C., & Devriendt, J. 2016, MNRAS,
    460, 2979
Wang, T., Yang, C., Wang, H., & Ferland, G. 2015, ApJ, 814, 150
Weymann, R. J., Morris, S. L., Foltz, C. B., & Hewett, P. C. 1991, ApJ,
    373, 23
Wildy, C., Goad, M. R., & Allen, J. T. 2015, MNRAS, 448, 2397
Xu, X., Arav, N., Miller, T., & Benn, C. 2018, ApJ, 858, 39